Key Points:
- We calculate dose and equivalent dose rates induced by galactic cosmic ray particles at varying heights above and below the Martian surface
- Different Martian regolith scenarios are simulated to understand the impact of subsurface components on the Martian radiation environment
- We find water/hydrogen-rich regolith may effectively reduce equivalent dose both above and below the ground via modulating the neutron flux

Correspondence to:
J. Guo,
jnguo@ustc.edu.cn

Subsurface Radiation Environment of Mars and Its Implication for Shielding Protection of Future Habitats

Lennart Röstel[1], Jingnan Guo[1,2,3] (ID) **, Saša Banjac[1]** (ID) **, Robert F. Wimmer-Schweingruber[1]** (ID) **, and Bernd Heber[1]** (ID)

[1]Institute of Experimental and Applied Physics, University of Kiel, Kiel, Germany, [2]School of Earth and Space Sciences, University of Science and Technology of China, Hefei, China, [3]CAS Center for Excellence in Comparative Planetology, USTC, Hefei, China

Abstract In order to quantify the optimal radiation shielding depth on Mars in preparation for future human habitats on the red planet, it is important to understand the Martian radiation environment and its dependence on the planetary atmospheric and geological properties. With this motivation we calculate the absorbed dose and equivalent dose rates induced by galactic cosmic ray particles at varying heights above and below the Martian surface considering various subsurface compositions (ranging from dry rock to water-rich regolith). The state-of-the-art Atmospheric Radiation Interaction Simulator based on GEometry And Tracking Monte Carlo method has been employed for simulating particle interaction with the Martian atmosphere as well as subsurface materials. We calculate the absorbed dose in two different phantoms: a thin silicon slab and a water sphere. The former is used to validate our model against the surface measurement by the Radiation Assessment Detector on the Curiosity rover, while the later is used to approximate a human torso, also for evaluation of the biologically weighted equivalent dose. We find that the amount of hydrogen contained in the water-rich regolith plays an important role in reducing the equivalent dose through modulation of neutron flux (below 10 MeV). This effective shielding by underground water is also present above the surface, providing an indirect shielding for potential human explorations at this region. For long-term habitats seeking the Martian natural surface material as protection, we also estimate the optimal shielding depth, for different given subsurface compositions, under maximum, average, and minimum heliospheric modulation conditions.

Plain Language Summary Space radiation is a major risk for humans, especially for manned missions in deep space and to Mars which does not have an atmosphere thick enough to shield against cosmic high-energy particles. It is practical and likely for future human habitats on Mars to use natural surface material as shielding protection against radiation. In order to quantify the optimized shielding depth, we model the radiation environment including the absorbed dose and biological equivalent dose induced by omnipresent galactic cosmic rays reaching Mars' surface and also subsurface. We also implement different Martian regolith properties in the model and compare the results. For instance, to limit the annual equivalent dose to be within 100 mSv, the required shielding depths are between 80 cm and 2.5 m depending on the soil composition with hydrated soil requiring less shielding. This is because water (hydrogen)-rich regolith may effectively reduce equivalent dose both above and below the Martian ground via modulating the flux of fast neutrons (with energy below 10 MeV). In conjunction with the new discovery of subsurface liquid water by Mars Express, our result suggests the advantage of seeking for human landing sites with high water content is also effective for radiation-shielding protection purposes.

1. Introduction

The visit of humankind to the planet Mars is considered as a major step for the future exploration of space. However, due to the thin Martian atmosphere compared to that of Earth and the lack of a global magnetic field (Acuña et al., 1998), highly energetic cosmic radiation is able to penetrate through the Martian atmosphere and even into the subsurface. The main contributors to this cosmic radiation are omnipresent galactic cosmic rays (GCR) and sporadic solar energetic particles (SEP). While both types of energetic particles may impose risks for deep space and planetary missions, the more variable and temporary SEP events generally

contain lower energy particles compared to GCR and therefore can be more easily shielded by the Martian atmosphere. For instance, at Gale Crater (with an average column depth of 21 g/cm^2) the atmosphere can stop primary protons below $\sim$ 160 MeV (which is the atmospheric cutoff energy) from arriving at the surface of Mars (Guo, Wimmer-Schweingruber, et al., 2019). GCR particles have energies from less than 1 MeV/nuc up to hundreds of TeVs with a power law distribution at energies above $\sim$ GeV/nuc (Allkofer, 1975) and are mainly composed of protons (87%) and helium (12%) and a low frequency of heavier nuclei (1%) (Simpson, 1983). GCR particles with energies higher than the Martian atmospheric cutoff energy can penetrate through the atmosphere and induce radiation on the surface of Mars. These particles, especially the ones with high charges and mass, can also interact with the atmosphere and regolith via fragmentation and spallation process generating secondary particles which also contribute to the radiation environment on Mars (e.g., Saganti et al., 2004). Due to their omnipresent nature, GCRs present as a continuous radiation background in space and on the surface of Mars. This long-term radiation exposure in space and on Mars has been considered as one of the main risks for future exploration missions (Cucinotta & Durante, 2006).

To evaluate the radiation risks for future human exploration of Mars, the Radiation Assessment Detector (RAD, Hassler et al., 2012) was designed to detect and analyze the most biologically hazardous energetic particle radiation during the cruise to Mars and on the Martian surface as part of the Mars Science Laboratory (MSL, Grotzinger et al., 2012). Since August 2012, MSL/RAD has provided the first assessment of the radiation environment on the Martian surface (Hassler et al., 2014) which is fundamental for evaluating the radiation risks and the consequent biologic effects likely to be encountered during a typical Mars mission. The result of the MSL/RAD measurement is also important for particle transport model validation (Guo, Banjac, et al., 2019; Matthiä et al., 2016) which can be used to evaluate and extrapolate the radiation environment at the subsurface layer of Mars. This is particularly important for future human explorations to Mars during which the Martian regolith has been considered as the most convenient shielding material against the cosmic ray radiation. Therefore, assessing the shielding depth as well as the composition of Martian surface material and their impact on the Martian subsurface radiation environment could provide valuable information on optimized shielding strategies for future human missions to Mars.

In previous studies, Dartnell et al. (2007) modeled the radiation exposure on a µm layer of water on and below the surface of Mars and calculated survival time for possible microbiological live forms. They found that the abundance of subsurface water ice can significantly reduce dose rates recorded in the water slab below the surface of Mars. However, the implications for a more human-like phantom are still to be examined.

In this work, at varying depths in the Martian atmosphere and in particular beneath the surface we model the GCR induced radiation dose rate as recorded both in a silicon slab (of 300 µm thickness, similar to that of MSL/RAD) and a water sphere phantom with a radius of 15 cm. To do so, we employ the state-of-art Atmospheric Radiation Interaction Simulator (AtRIS) toolkit (Banjac et al., 2019) based on GEANT4 (GEometry And Tracking) which is a Monte Carlo approach widely used for simulating the interactions of particles as they traverse matter (Agostinelli et al., 2003; Allison et al., 2006, 2016). AtRIS models the interactions of cosmic particles with planetary atmosphere and soil and has been applied to the Martian environment with the calculated surface particle spectra validated against the MSL/RAD measurements (Guo, Banjac, et al., 2019). In the current study, we further validate the absorbed dose rate in the silicon slab against the surface RAD measurements, and then we apply our model with various types of subsurface materials and water contents to investigate the impact of the regolith composition on the subsurface radiation environment at different depth. The result of this study provides references shielding strategies for potential future habit on Mars.

2. Model Description and Implementation

2.1. The Mars Surface and Subsurface Environment

For the purpose of simulating the interactions of energetic particles through the Martian atmosphere and regolith, we employ the state-of-the-art Mars Climate Database (MCD, http://www-mars.lmd.jussieu.fr, Lewis et al., 1999) describing the physical properties and composition of the Martian planetary environment. MCD (version 5.3 used here) generates the altitude-dependent data for atmospheric pressure, density, temperature, and chemical composition in a similar approach used in Guo, Banjac, et al. (2019). For the purpose of validating the model against the RAD data, we use data extracted from MCD based on Gale Crater (coordinate: 4.5°S, 137.4°E), yielding a surface elevation of −4.4 km in the Mars Orbiter Laser Altimeter coordinate.

Table 1

Elemental Compositions and Densities of the Dry Subsurface Scenarios: Quartz (SiO$_2$), Basaltic Andesite Rock (AR), Sandstone (SS), and Sulfur Concrete (SC)

Dry scenarios	Mass fraction (%)				Density (g/cm^3)
	O	Si	Fe	Other	
Quartz (SiO$_2$)	53	47	0	0	2.8
Andesite rock (AR)	44	27	12	17	2.8
Sandstone (SS)	41	21	20	18	2.2
Sulfur concrete (SC)	22	10	8	60 (51% S)	2.0

Note. All compositions were normalized to 100%.

In order to model the Martian atmosphere in a realistic as well as efficient manner, 80 altitude steps were spaced evenly in logarithmic scale up to 80 km, accounting for the exponential decrease in pressure with increasing height. The elemental composition of the Martian atmosphere consists of C, O, N, Ar, and H with more than 95% of the molecules being CO_2. Although the surface pressure changes daily and seasonally up to about 25% at Gale Crater (Haberle et al., 2014), we use a surface pressure of 781 Pa, corresponding to a vertical column depth of 21 g/cm^2. This pressure is close to the average value of the first 300 sols of MSL's measurement on Mars during which the RAD measurement is used to validate our modeled result as shown later.

We employ seven different subsurface scenarios, with specific densities and compositions. Two distinct rock types, of which outcrops have been analyzed at different landing sites, as well as two artificial subsurface compositions have been chosen in the scope of this work:

1. An iron rich sandstone (SS) as analyzed by "ChemCam" on board of Curiosity at the Cooperstown outcrop (Le Deit et al., 2016). As a typical value for sandstone on Earth (Manger, 1963), we use a bulk density of 2.2 g/cm^3 for SS.
2. A basaltic andesite rock type (AR) analyzed at the Pathfinder site and calculated as the soil-free rock by Wänke et al., (2001). It has intermediate quartz content of 57% by weight and a high density of 2.8 g/cm^3.
3. Quartz (SiO$_2$) as a major component of all igneous rocks found on Mars and on Earth. As it is normally not present in its pure form, this is a simplified scenario for the Martian rocks.
4. Sulfur concrete (SC) as an ideal material for the construction of future buildings on Mars (Wan et al., 2016). It consists of 50% sulfur and 50% Martian soil by weight with an estimated density of 2.0 g/cm^3.

Mitrofanov et al. (2004) estimated the soil water (hydrogen) contents for numerous locations on Mars based on Mars Odyssey spacecraft measurements of the epithermal neutron flux in orbit of Mars. Due to the effective moderation of fast neutrons by hydrogen, the flux of neutrons with epithermal energies is anticorrelated to the amount of hydrogen and therefore water ice in the soil. Based on these water content estimations, another three scenarios with subsurface water ice have been implemented in this work:

5. A homogeneous mixture of 50% water and 50% basaltic andesite rock by weight (W50) as a presumably realistic scenario for the Martian north pole, yielding a bulk density of 1.4 g/cm^3.
6. A homogeneous mixture of 10% water and 90% basaltic andesite rock by weight (W10), corresponding to a bulk density of 2.4 g/cm^3.
7. An inhomogeneous scenario for Arabia Terra (AT), where a soil mixture of 10% water by weight underlies 30 g/cm^2 of dry rock. This scenario is believed to be realistic for some nonpolar locations on Mars, that is, Arabia Terra (Mitrofanov et al., 2004).

The chemical components have been converted into an elemental composition (to be applicable to the particle transport modeling by AtRIS) as shown in Tables 1 and 2 for the dry and hydrated scenarios, respectively.

2.2. Model Description: AtRIS

As GCRs are charged particles propagating into the heliosphere, they are modulated by the heliospheric magnetic field, which varies during different solar activities. While the flux of particles with energies below a few GeV/nuc is more attenuated during enhanced solar activities, particles with higher energies are less affected by the magnetic field. The Badhwar O'Neil (BON, O'Neill, 2010) model, employed in this work,

Table 2
Bulk Densities and Mass Fractions of Hydrated Scenarios Containing Water: 50% of Hydrogen (W50) by Weight, 10% of Hydrogen by Weight (W10), and the Inhomogeneous Scenario Arabia Terra (AT)

Hydrated scenarios	Water by weight (%)	Rock by weight (%)	Density (g/cm^3)
10% water & 90% andesite rock (W10)	10	90	2.4
50% water & 50% andesite rock (W50)	50	50	1.4
Arabia Terra (AT)			
Above 30 g/cm^2	0	100	2.8
Below 30 g/cm^2	10	90	2.4

describes the energy loss of GCR particles taking into account diffusion, convection, and adiabatic deceleration of these particles from the outer edge of the heliosphere into the vicinity of about 1 AU. A solar modulation parameter Φ positively correlated with solar activity is used as the input parameter of the model for obtaining GCR particle spectra (of different particle types) during different solar modulation conditions. Typical values for solar modulation parameter Φ in the BON model range approximately from $\Phi = 400$ MV for solar minima to $\Phi = 1,000$ MV for solar maxima.

The propagation of primary GCR particles through the Martian environment is then calculated by AtRIS as illustrated in Figure 1. The geometric setup of Mars used in this work comprises a total of 121 spherical concentric shells. The outer 80 shells represent atmospheric sheets as retrieved from the MCD as described in section 2.1. The inner 40 sheets represent the subsurface layers evenly distributed in logarithmic scale from 1 cm to 10 m below the surface of Mars. Except for the Arabia Terra scenario, all subsurface layers were constructed homogeneously in composition and density at different depth. At the interface between two adjacent atmospheric or subsurface layers differential particle fluxes of a variety of particle species are calculated employing an atmospheric response matrix approach as described in Guo, Banjac, et al. (2019).

In terms of radiation effects, an important quantity (from both measured and modeled results) is the absorbed dose which describes the energy deposited by all energetic particles (both charged and neutral) as they transverse through matter normalized to the mass of the matter. It has the unit of gray which is equivalent to J/kg. As described above, we obtain the particle spectra (of different species) at certain atmospheric/regolith depth. These particles are then used to calculate the induced dose considering different
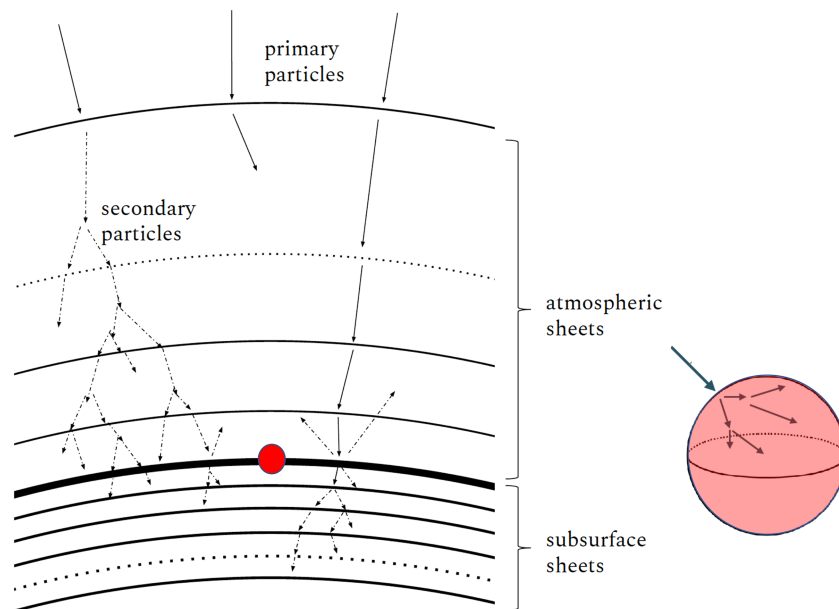
Figure 1. Illustration of the AtRIS model setup as a chain effect starting from the primary particles impinging into, propagating through, and interacting with the Martian atmosphere and regolith (left). At the interfaces between successive planetary layers, the dose rate induced by the corresponding particle fluxes are calculated inside a spherical phantom (right), which is one of the two phantoms used in this study.

phantoms embedded at this planetary layer. The same particle spectra may induce different absorbed doses in different phantoms (such as a detector, a biological structure, or even a human body) due to different material properties as well as the geometry, especially the size, of the phantom. This is because larger phantoms can more easily stop ions inside, and the interaction with incoming particles to generate secondaries is also more likely as shown in the right panel of Figure 1. For the calculation of absorbed dose in different phantoms, AtRIS offers the possibility to use precalculated phantom response matrices (converting particle spectra to dose) as described in Banjac, Berger, et al. (2019). In this work, we calculate the absorbed dose induced in two different phantoms: a water sphere phantom with a radius of 15 cm and a simplified model approximating the composition and dimension of the human torso and a silicon slab of 300 μm thickness (as a comparison with the RAD dosimetry silicon detector).

In addition, with the first water sphere phantom, we also calculate the equivalent dose as defined by the International Commission on Radiological Protection (ICRP, 2010). It has the unit of sievert (Sv) and describes the biological effectiveness of the absorbed dose by applying a weighting factor which depends on incident particle types and energies in the case of neutrons. These factors are shown in Table 2.1 and Figure 2.1 of the ICRP reference and are mostly 1 or 2 for light particles such as photons, electrons, protons, muons, and pions. They are as large as 20 for particles heavier than helium ions and neutrons around 1 MeV. However, we note that equivalent dose is a quantity generally used in radiation protection, thus giving an upper bound of the biological effectiveness of the radiation incident on humans, derived from legal concerns related to radiation protection standards. For space dosimetry applications, another quantity called "dose equivalent" (also in unit of Sv) is often assessed, as in the case of RAD measurement. It is determined as the multiplication of detected absorbed dose converted in water and a mean biological quality factor. The latter is dependent on the measured histogram of linear energy transfer, which is the mean energy loss by charged particles due to electronic interactions per unit path length. Concerning the protection of future astronauts on Mars, the equivalent dose employed in the current study is rather an overestimation of the maximal potential hazard of the calculated radiation exposure in comparison to the radiation risk defined through dose equivalent.

As hydrogen and helium particles contribute to the majority of GCRs and the high computational need of heavier ions, most of our simulations comprise only hydrogen and helium primary GCR particles. But for one of seven scenarios, we also simulated additional heavier primary GCR particle species as discussed in section 3.1 to estimate the importance of their contribution. In each simulation, all relevant secondary particle species contributing to dose are considered, which are p, $\bar{p}$, n, $\bar{n}$, e^-, e^+, γ, μ^+, μ^-, π^+, π^0, π^-, K^+, K^-, ^{2}H, ^{3}H, ^{3}He, ^{4}He, ^{7}Li, and heavier nuclei up to ^{58}Ni.

For each primary particle type, we use a total input of 50 bins of energy between 1 MeV and 1 TeV evenly distributed in a logarithmic scale, with the exception of protons for which 60 bins were used for the energy range of 1 MeV to 10 TeV. At a given sheet interface S, the absorbed dose $d_{\epsilon,S}^{(p)}$ and equivalent dose $h_{\epsilon,S}^{(p)}$, as defined earlier, are calculated as the average value per input particle of type p in each energy bin ϵ. The calculated $d_{\epsilon,S}^{(p)}$ and $h_{\epsilon,S}^{(p)}$, with units of Gy/particle and Sv/particle, respectively, are then scaled with a given input flux at the top of the atmosphere as follows. Let $I_\epsilon^{(p)}(\Phi)$ in units of particles/m^2/sr/s/MeV be the GCR induced differential flux which is also a function of the solar modulation parameter Φ. The total number of particles $N_\epsilon^{(p)}(\Phi)$ of type p incident on top of the atmosphere per second can then be calculated as

$$N_\epsilon^{(p)}(\Phi) = I_\epsilon^{(p)}(\Phi) A_{top} \delta_\epsilon \pi, \tag{1}$$

where $A_{top} = 4\pi R_{top}^2$ is the area of the outermost atmospheric shell with a radius $R_{top} = 3,\ 471.1$ km and δ_ϵ is the energy bin width. As the input particles were produced isotropically inward from the source sphere, π is the integration of the cosine of the zenith angle (Sullivan, 1971). The total absorbed dose rate $D_S(\Phi)$ and equivalent dose rate $H_S(\Phi)$ as recorded in a phantom at sheet interface S is the sum over all energy bins ϵ and particle types p:

$$D_S(\Phi) = \sum_p \sum_\epsilon N_\epsilon^{(p)}(\Phi) d_{\epsilon,S}^{(p)} \tag{2}$$

$$H_S(\Phi) = \sum_p \sum_\epsilon N_\epsilon^{(p)}(\Phi) h_{\epsilon,S}^{(p)} \tag{3}$$
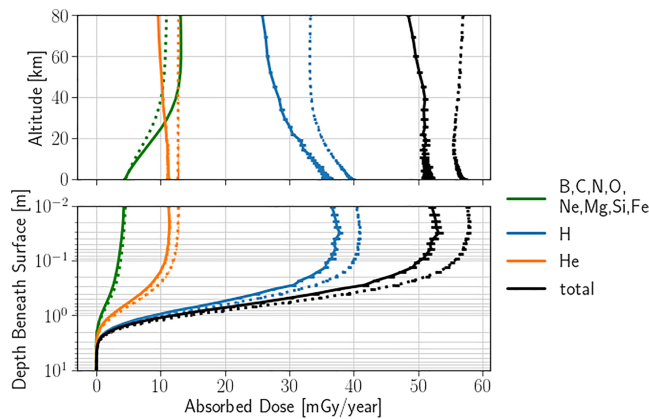
Figure 2. Primary particle species contribution to absorbed dose rates in the water sphere (dashed) and silicon slab (solid). Hydrogen (blue), helium (orange), and the eight simulated heavier primary particle species (green) are summed up to the total absorbed dose (black).

During the above procedure, we also propagate the statistical errors from the Monte Carlo calculations in a similar manner as described in Guo, Banjac, et al. (2019).

3. Validation and Results

As validated in our previous work (Guo, Banjac, et al., 2019) comparing the AtRIS-modeled fluxes of various hydrogen and helium isotopes against RAD measurements, the FTFP_INCLXX_HP physics list has been found to best describe the particle transport process in the Martian environment and thus is used in the current study. In addition, we validate the AtRIS-calculated dose rate in this work by comparing the absorbed dose rate in the silicon slab with the RAD measurement. During the first 300 sols after landing of MSL, RAD measured the surface dose rate 58 ± 5 mGy/yr in the silicon detector under an average solar modulation parameter of about 580 MV and a mean column depth of 21 g/cm^2 (Hassler et al., 2014). Assuming similar GCR and atmospheric conditions, our modeled surface dose rate in the silicon slab is 51.6 ± 0.6 mGy/yr as shown in Figure 2. This agrees approximately with the data within the lower standard deviation or 11%. The absorbed dose in the water sphere phantom is in all cases 10–16% higher compared to the silicon slab phantom, which can be explained by the higher ionization energy loss of charged particles in water and by the increased sensitivity to neutrons in the water sphere (e.g., Banjac et al., 2019).

### 3.1. Radiation Contribution by Different Primary Particle Types

When comparing radiation environments at different elevations, evaluating the contribution by different primary particle types of the GCRs can provide valuable information about most relevant particle species and energy ranges for optimizing the computational efficiency in future simulations. In the scenario of dry andesite rock surface condition, we simulate primary proton, helium, and another eight higher-Z GCR species (B, C, N, O, Ne, Mg, Si, and Fe, which are the most abundant ones in GCR heavy ions) and evaluate their respective contributions to the absorbed dose in the two phantoms at different shielding depth as shown in Figure 2. The GCR spectra are generated from the BON model with a solar modulation parameter of 580 MV for the purpose of model validation as explained earlier.

The blue lines in Figure 2 show that the primary GCR proton contributed absorbed dose rate increases with increasing atmospheric depth. A maximum is reached at a depth of 3 cm beneath the surface, from where the proton-induced dose rate declines with increasing depth. This can be explained by two concurrent effects: as primary protons traverse through the atmosphere, they lose energy by ionization and excitation of the target material and by the production of secondary particles that further contribute to dose rates themselves. However, primary particles with higher Z values tend to fragment more often in the atmosphere and in general have a smaller penetrating depth through ionization energy loss. As shown, the total absorbed dose rate induced by primary high Z GCRs steadily decreases with increasing depth. For primary protons, particles with energy larger than 178 ± 21 MeV contribute more than 97% of the surface dose rate, while for primary irons, this cutoff energy is 35 ± 5 GeV (or 620 ± 90 MeV per nucleus).

On the surface of Mars, the largest fraction of absorbed dose in both phantoms is induced by primary hydrogen (about 69–70%) and helium (about 22%) GCR particles. In the silicon slab, the higher-Z primary particles contribute 9% of absorbed dose rate on the surface of Mars. This ratio is slightly lower in the water sphere, being about 8%.

Figure 3 shows proton-contributed equivalent dose rate increases with increasing atmospheric depth, more evidently than that in Figure 2, and also increases with the regolith depth. A peak is evident at a depth of 30 cm beneath the surface. In comparison to the absorbed dose rate in the water sphere in Figure 2, this more significant increase of the
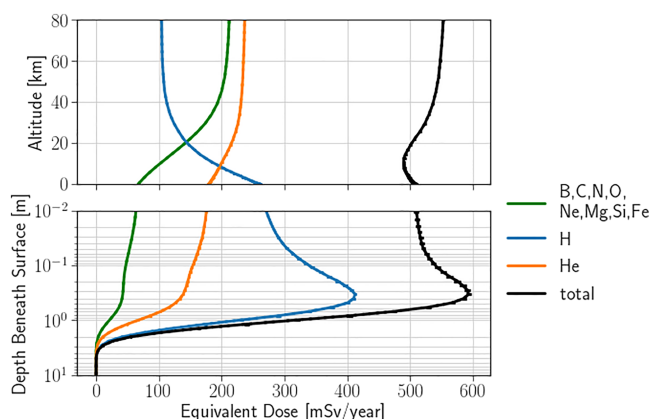
Figure 3. Primary particle species contribution to equivalent dose rates in the water sphere.
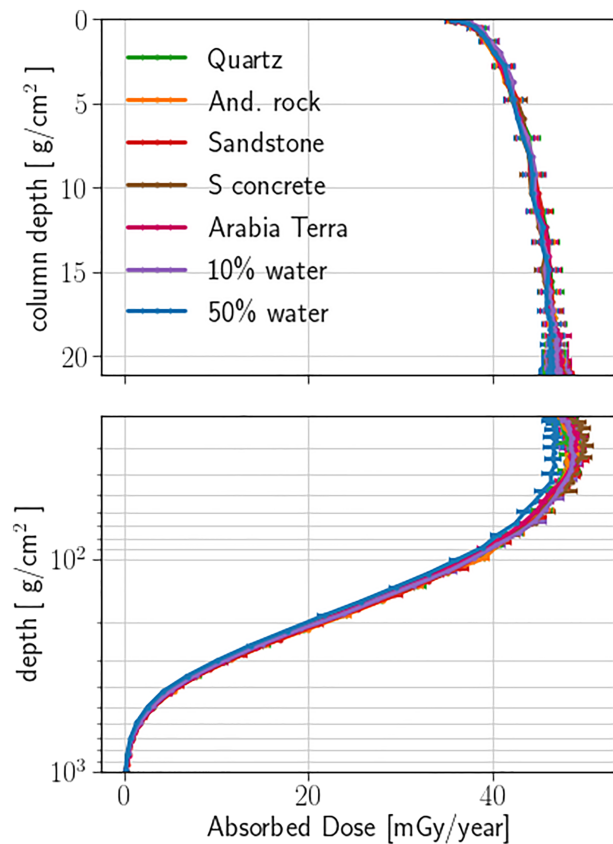
Figure 4. Absorbed dose in the silicon slab versus the Martian atmospheric and regolith depth (in unit of g/cm^2) under the different subsurface scenarios.

proton-contributed equivalent dose rate with depth can be explained by a drastic increase of the generation of secondary particles with a higher radiation weighting factor, in particular neutrons as shown and discussed later. For the total equivalent dose rate, a peak is also present at a depth of 30 cm beneath the surface.

3.2. The Influence of Different Regolith Properties

Based on seven different regolith properties as discussed in section 2, we calculate and compare different radiation environments therein. When analyzing the shielding effects imposed by the different subsurface materials, one has to carefully take into consideration the type of phantom in which the absorbed dose is evaluated.

As discussed in the last section, primary hydrogen and helium particles contribute the majority amount, more than 90%, of the Martian radiation environment, we simulate only these two primary particle types for the following scenarios, also to save computational power.

Figure 4 shows the modeled absorbed dose rate as recorded in the silicon slab for the seven subsurface scenarios. The shielding depth is expressed in units of g/cm^2 which is to be noted different from the actual atmospheric/regolith height. There is no significant difference between the absorbed dose rates under different shielding properties within the uncertainty of the statistics. If at all, there is only a slight decrease in the absorbed dose under the 50% water rock mixture. For all other materials, a maximum absorbed dose rate is reached at approximately 30 g/cm^2 of shielding depth (including atmospheric column depth) in the subsurface.

Figure 5 shows the absorbed dose rate in the water sphere phantom versus the height (not the column depth) of the Martian environment for seven different subsurface scenarios. The adoption of different units of atmospheric depth in Figures 3 and 4 reflects the difference in densities of various regolith considered. A slightly but statistically significant attenuation can be observed in the top centimeters of subsurface materials with contents of surface water (i.e., 10% of water and 50% of water). As this reduction in absorbed dose extends to elevations above the surface while the atmospheric composition is the same for different scenarios, this can only be explained by the difference of upward directed particle fluxes in different regolith scenarios. On the surface, the abundance of subsurface water yields a minor reduction in absorbed dose rates of 5% for W50 and 3% for W10 compared to other scenarios. However, at deeper subsurface depth, as better shown in the magnified panel, the dry rock materials have slightly more shielding than the water mix materials due to their higher bulk densities.

Figure 6 shows the equivalent dose rates in the water sphere phantom versus height. As shown, the advanced shielding effect of subsurface materials containing water is drastically increased. The Martian surface equivalent dose reduces by about 45%, 36%, and 27% for the 50% water, 10% water, and Arabia Terra scenarios, respectively, as compared to the dry andesite rock scenario. Furthermore, a significant alteration of equivalent dose is visible up to the top of the atmosphere. Again, this has to be explained by a reduction of upward directed particle fluxes. Within the top meter of subsurface material, the improved shielding effect is preserved for all water scenarios despite of the lower density. The inhomogeneous Arabia Terra scenario is remarkable in that it shows a considerable reduction even in equivalent dose rates in the top dry layer at 0–11 cm below the surface. Below this depth, the Arabia Terra scenario contains 10% water, equivalent to the W10 scenario. At about 40 cm, the shielding effect of the Arabia Terra scenario becomes almost the same as that of the W10 scenario.

In order to explain the observed anticorrelation of subsurface water abundance and equivalent dose, differential fluxes of all secondary particle species contributing to dose have been calculated. Figure 7 shows the surface neutron flux of the 50% water, 10% water, and andesite rock scenarios, respectively. We notice a drastic decrease in neutron fluxes below about 10 MeV for the first two hydrated scenarios. On the y axis, the differential neutron flux dF/dE is multiplied by the energy of the neutron itself which is the maximum
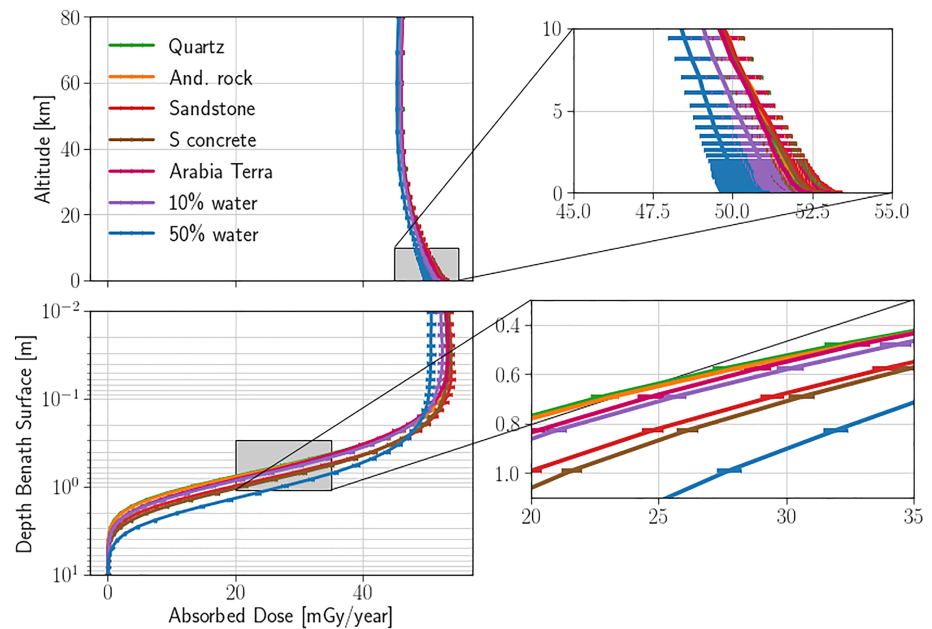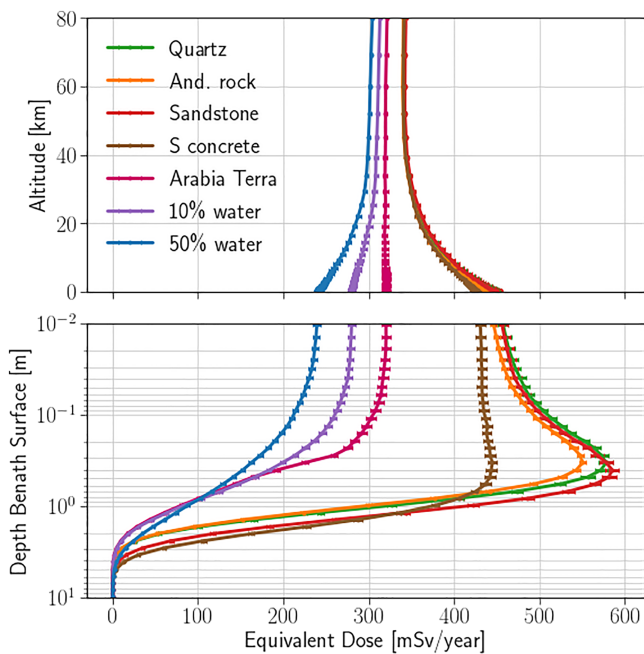
Figure 5. Absorbed dose in the water sphere versus the Martian atmospheric and regolith depth (in unit of km and m for above and below the surface, respectively) under the different subsurface scenarios. The regions above surface up to 10 km and from 0.3 to 1.1 m below the surface are magnified.

energy that neutron can deposit in a phantom, thus more related to the definition of dose. The neutron flux extends up to an energy of 10 TeV, corresponding to the maximal primary proton energy due to the conservation of momentum during nearly elastic hadronic processes. While surface neutron fluxes above energies of about 10 MeV are not significantly influenced by the concentration of subsurface water, at lower energies a stronger attenuation is observed. When compared to the dry andesite rock scenario, neutron fluxes are reduced by factors of approximately 2 and 5 at around 1 MeV for W10 and W50 scenarios, respectively. The reduction factors are even bigger at lower energies. As defined by ICRP (2010), 1 MeV neutrons have the largest biological weighting factor (more than 20) compared to other neutron energies or particle species, the attenuation of the neutron flux around this energy under the hydrated scenarios significantly reduces the equivalent dose.

The strong attenuation of neutron fluxes by high contents of subsurface water can be explained by the following effects: Due to the high concentration of hydrogen in water scenarios, incident fast neutrons frequently undergo efficient elastic scattering. These slowed-down neutrons are then more easily captured by hydrogen, with the emission of gamma rays. These scattered neutrons are thermalized by the subsurface hydrogen and are thus less likely to reach the surface. This leads to an indirect shielding effect even on and above the surface in water-rich scenarios compared to dry scenarios. Alternatively, surface spectra of other major particle species, especially ions, do not seem to depend on subsurface water contents. This is mainly because they are mostly primary particles and secondary particles generated in the atmosphere and the albedo contribution to the high-Z fluxes from the soil is comparably small. Besides, the biological weight of light particles, such as protons or photons, contributing to equivalent dose is much less compared to that of neutrons around 1 MeV. As a result, the equivalent dose differs by about 45%

Figure 6. Absorbed dose in the water sphere versus the Martian atmospheric and regolith depth (in unit of km and m for above and below the surface, respectively) under the different subsurface scenarios.
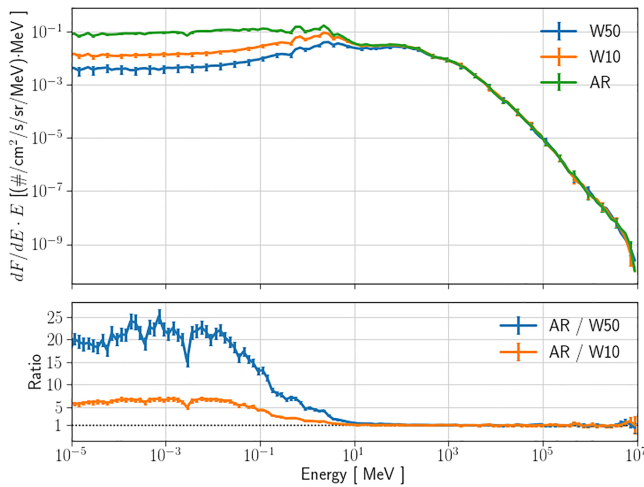
Figure 7. Comparison of surface neutron fluxes modeled using different surface materials. W50 stands for 50% water content in the andesite rock, and W10 stands for 10% water in the andesite rock. AR represents andesite rock. (top) Differential neutron flux dF/dE multiplied by neutron energy E versus the neutron energy. (bottom) Ratio of differential fluxes.

between W50 and dry scenarios on the surface (and up to 75% in the sub-surface) as shown in Figure 6 and it can be concluded that equivalent dose in the water sphere are heavily dominated by the contribution of neutrons.

The dry subsurface materials of andesite rock, sandstone, and quartz in Figure 6 show an increase in equivalent dose rates with depth reaching a peak at about 30–40 cm or 88–102 g/cm^2 depth, with an exception of sulfur concrete for which there is no considerable change in the equivalent dose rate within approximately the upper 50 cm of subsurface material. Note that these calculations of equivalent dose only include H and He primary particle species. The additional contribution of heavier ions to the equivalent dose rate in the water sphere can be considered to be in the order of $\sim 10\%$ according to the calculations of the andesite rock scenario (section 3.1).

Equivalent doses $H_S(\Phi)$ under a given solar modulation parameter of 580 MV are linearly interpolated between subsurface sheets and intersections for given values of equivalent doses can be obtained. In Table 3 we show the required shielding depths for a few examples of equivalent dose reducing to certain values. This table provides references of shielding strategies for potential future habit on Mars. From the table, one can choose the optimal shielding material (with the least amount of required shielding depth) under a specific requirement of equivalent dose. For instance, for equivalent dose reductions down to 200 mSv/yr, the 50% water scenario is optimal. To reduce equivalent dose rate down to values smaller than about 100 mSv/yr, the Arabia Terra and W10 subsurface scenarios are favorable, providing relatively higher densities than W50.

3.3. The Influence of Heliospheric Modulation

In sections 3.1 and 3.2, a fixed and medium solar modulation parameter has been employed, in order to compare the results with the RAD measurements under similar heliospheric conditions. However, absorbed dose and equivalent dose can be strongly affected by variations of the primary GCR flux which is modulated by the heliospheric activities. Weaker solar modulations (smaller values of Φ) generally result in higher GCR fluxes in space and consequently also on and below the surface of Mars as observed by the MSL/RAD at Gale Crater (Guo et al., 2015). Here we use typical values of $\Phi = 400$ MV, $\Phi = 580$ MV, and $\Phi = 1,000$ MV representing weak, average, and very strong solar modulation conditions, respectively. For an equivalent dose rate reduction down to (a) 200 mSv/yr which is less than half of the surface equivalent dose rate under dry scenarios during medium solar modulation condition and (b) 100 mSv/yr which is considered as the boundary above which increased lifetime cancer is evident, the required shielding depths under different subsurface scenarios are shown in Figure 8. As expected, during solar maximum conditions when GCR fluxes are much lower, significantly less shielding material is needed for all subsurface scenarios. In fact no

Table 3
Required Shielding Depth for Reduction of Equivalent Dose Rate to a Given Value in the Water Sphere

Equivalent dose per year (mSv)	Required subsurface shielding depth (cm)					
	AR	SS	SC	AT	W10	W50
400	79 ± 1	105 ± 1	89 ± 3	None	None	None
300	100 ± 1	131 ± 1	137 ± 2	14 ± 3	None	None
200	126 ± 1	164 ± 1	184 ± 1	39 ± 1	34 ± 1	16 ± 1
100	167 ± 1	215 ± 2	248 ± 2	84 ± 2	87 ± 1	87 ± 1
50	205 ± 1	265 ± 3	305 ± 3	133 ± 2	137 ± 2	164 ± 3
10	295 ± 3	377 ± 6	432 ± 6	240 ± 3	243 ± 3	334 ± 6

Note. AR = andesite rock; SS = sandstone; SC = sulfur concrete; AT = Arabia Terra; W10 = 10% water in the andesite rock; W50 = 50% water mixture with andesite rock. Solar modulation condition is $\Phi = 580$ MV. "None" means no shielding is needed.
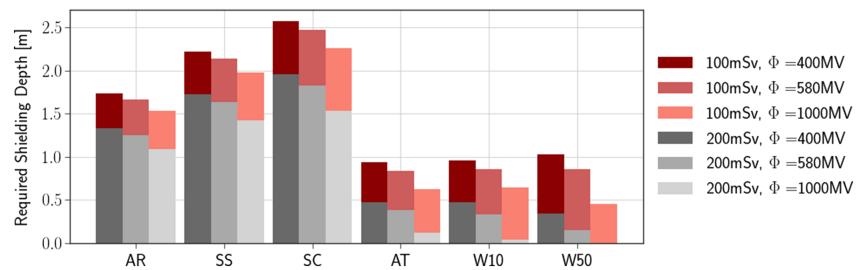
Figure 8. Required subsurface shielding for peak ($\Phi = 1,000$ MV), average ($\Phi = 580$ MV), and weak solar modulation ($\Phi = 400$ MV) scenarios. Gray and Red bars show the required shielding depths for achieving an equivalent dose reduction to 200 mSv/yr and 100 mSv/yr, respectively.

shielding is needed during the peak of solar maximum condition of $\Phi = 1,000$ MV for W50 in case (a). It is also clearly shown that the surface materials with water content require much less shielding depth than the dry regolith conditions.

4. Summary and Discussion

In order to better understand the Martian radiation environment and its dependence on the planetary atmospheric and geological properties, we calculate GCR-induced absorbed dose and equivalent dose rates at varying heights above and below the Martian surface considering various subsurface compositions using the state-of-the-art GEANT4/AtRIS code. Seven different regolith scenarios are implemented based on in situ measurements of the surface composition and possible water (hydrogen) content estimated by remote-sensing observations. We also include two different phantoms for calculating the absorbed dose: a 300-μm-thick silicon slab and a 15-cm-radius water sphere. The silicon phantom is used for benchmarking the calculations against the surface RAD measurement. Because human tissue consists to a large extent of water, the water sphere phantom is a closer approximation for evaluating the radiation risks for the human body. We note that critical risk estimations, such as the effective dose taking into consideration of the organs distributed within the body, would require the use of anthropomorphic phantoms and further validations. The quantity equivalent dose in this study is rather an upper estimation of the radiation risk and is used mainly for demonstrating the dependence of radiation on subsurface shielding properties.

For both phantoms, the absorbed dose versus depth distribution has very little difference among different regolith scenarios as shown in Figures 4 and 5. On the other hand, equivalent dose rates calculated in the water sphere phantom both above and below surface vary strongly depending on the water content in the subsurface material. Only a minor dependence of the equivalent dose on the exact dry rock composition has been observed and the equivalent dose increases in the first ~200 g/cm² (0.7–0.9 m) of soil depth, as shown in Figure 6. This can be considered as the minimum shielding depth for potential human habits based on dry rocky subsurface materials on Mars. In fact any "shielding" thickness smaller than this value may even enhance the equivalent dose resulting in a worsened radiation environment compared to the surface case.

Alternatively, medium to large amounts of subsurface water ice (10–50% by weight) are highly favorable both for direct shielding below the surface and indirect shielding above the surface. The enhanced shielding effect due to the water content in the surface material can be explained by the attenuation in neutron fluxes below 10 MeV as shown in Figure 7, due to the enhanced biological weighting factor of neutrons at this energy range contributing to the equivalent dose. This highlights the importance of carefully examining the neutron spectra and efficiently reducing the neutron flux for providing a better shielding environment of future human habitats on Mars.

Regolith-based shielding could be provided even by several natural geological features, offering potential habitats for humans staying on Mars. Observations from the orbit of Mars revealed that possible cave skylights (Cushing et al., 2007) or lava tubes (Léveillé & Datta, 2010) could potentially provide shelter from cosmic radiation. Moreover, according to this study, enhanced content of water ice in the subsurface can efficiently reduce the equivalent dose due to the moderation and absorption of biological effective neutrons by hydrogen. Even above the surface without direct regolith-based shielding above, equivalent dose rate is evaluated to be reduced by about 36% with a homogenous subsurface water content of 10%. Mitrofanov et al. (2004) suggested that the highest water content on the planet can be expected at the cold polar and subpolar

regions of the north and south poles. Moreover, there are also some regions near the equator where relatively high contents of water underlie a dry top layer, that is, Arabia Terra and the Medusae Fossae. Recently, radar data collected by ESA's Mars Express point to a pond of liquid water buried under layers of ice and dust in the south polar region of Mars (Orosei et al., 2018). Because the surface equivalent dose rate is significantly reduced even with the dry top layer, as shown in the Arabia Terra scenario, these regions with high-water content might be preferable and realistic landing and habitat sites for reducing the radiation risk of a long-term stay on Mars.

Furthermore, the results presented in section 3.3 suggest that periods with high solar modulation conditions are generally better for reducing the GCR-induced Martian surface radiation. For solar maximum conditions ($\Phi = 1,\ 000$ MV) surface equivalent dose reduces by about 49–54%, depending on the subsurface material, compared to that of solar minimum conditions. We note that the risk for exposure to SEPs during solar maximum conditions could alternatively increase, which has not been accounted for in this study. However, since SEPs have generally lower energies (only up to 1–2 GeV in rare extreme events) than GCR particles, they are more easily to be shielded by the atmosphere and regolith. Thus, the shielding depth suggested by our study (i.e., shown in Table 3) against GCRs is also sufficient for shielding against SEPs.

References

Acuña, M. H., Connerney, J. E. P., Wasilewski, P., Lin, R. P., Anderson, K. A., Carlson, C. W., et al. (1998). Magnetic field and plasma observations at Mars: Initial results of the Mars Global Surveyor mission. *Science*, *279*(5357), 1676–1680. https://doi.org/10.1126/science.279.5357.1676

Agostinelli, S., Allison, J., Amako, Ka., Apostolakis, J., Araujo, H., Arce, P., et al. (2003). GEANT4—A simulation toolkit. *Nuclear instruments and methods in physics research section A: Accelerators, Spectrometers, Detectors and Associated Equipment*, *506*(3), 250–303. https://doi.org/10.1016/S0168-9002(03)01368-8

Allison, J., Amako, K., Apostolakis, J., Araujo, H., Arce Dubois, P., Asai, M., et al. (2006). GEANT4 developments and applications. *IEEE Transactions on Nuclear Science*, *53*(1), 270–278. https://doi.org/10.1109/TNS.2006.869826

Allison, J., Amako, K., Apostolakis, J., Arce, P., Asai, M., Aso, T., et al. (2016). Recent developments in GEANT4. *Nuclear Instruments and Methods in Physics Research A*, *835*, 186–225. https://doi.org/10.1016/j.nima.2016.06.125

Allkofer, O. C. (1975). Introduction to cosmic radiation. *NASA STI/Recon Technical Report A*, *75*, 46929.

Banjac, S., Berger, L., Burmeister, S., Guo, J., Heber, B., Herbst, K., & Wimmer-Schweingruber, R. (2019). Galactic cosmic ray induced absorbed dose rate in deep space—Accounting for detector size, shape, material, as well as for the solar modulation. *Journal of Space Weather and Space Climate*, *9*, A14. https://doi.org/10.1051/swsc/2019014

Banjac, S., Herbst, K., & Heber, B. (2019). The Atmospheric Radiation Interaction Simulator (AtRIS)—Description and validation. *Journal of Geophysical Research: Space Physics*, *124*, 50–67. https://doi.org/10.1029/2018JA026042

Cucinotta, F. A., & Durante, M. (2006). Cancer risk from exposure to galactic cosmic rays: Implications for space exploration by human beings. *The Lancet Oncology*, *7*(5), 431–435. https://doi.org/10.1016/S1470-2045(06)70695-7

Cushing, G. E., Titus, T. N., Wynne, J. J., & Christensen, P. R. (2007). THEMIS observes possible cave skylights on Mars. *Geophysical Research Letters*, *34*, L17201. https://doi.org/10.1029/2007GL030709

Dartnell, L. R., Desorgher, L., Ward, J. M., & Coates, A. J. (2007). Modelling the surface and subsurface Martian radiation environment: Implications for astrobiology. *Geophysical Research Letters*, *34*, L02207. https://doi.org/10.1029/2006GL027494

Grotzinger, J. P., Crisp, J., Vasavada, A. R., Anderson, R. C., Baker, C. J., Barry, R., et al. (2012). Mars Science Laboratory mission and science investigation. *Space science reviews*, *170*(1-4), 5–56. https://doi.org/10.1007/s11214-012-9892-2

Guo, J., Banjac, S., Röstel, L., Terasa, J. C., Herbst, K., Heber, B., & Wimmer-Schweingruber, R. F. (2019). Implementation and validation of the GEANT4/AtRIS code to model the radiation environment at Mars. *Journal of Space Weather and Space Climate*, *9*(A2), 19. https://doi.org/10.1051/swsc/2018051

Guo, J., Wimmer-Schweingruber, R. F., Grande, M., Hannah Lee-Payne, Z., & Matthia, D. (2019). Ready functions for calculating the Martian radiation environment. *Journal of Space Weather and Space Climate*, *9*(A7), 11. https://doi.org/10.1051/swsc/2019004

Guo, J., Zeitlin, C., Wimmer-Schweingruber, R. F., Rafkin, S., Hassler, D. M., Posner, A., et al. (2015). Modeling the variations of dose rate measured by RAD during the First MSL Martian year: 2012–2014. *The Astrophysical Journal*, *810*(1), 24. https://doi.org/10.1088/0004-637X/810/1/24

Haberle, R. M., Gómez-Elvira, J., Torre Juárez, M., Harri, A. M., Hollingsworth, J. L., Kahanpää, H., et al. (2014). Preliminary interpretation of the REMS pressure data from the first 100 sols of the MSL mission. *Journal of Geophysical Research: Planets*, *119*, 440–453. https://doi.org/10.1002/2013JE004488

Hassler, D. M., Zeitlin, C., Wimmer-Schweingruber, R. F., Böttcher, S., Martin, C., Andrews, J., et al. (2012). The Radiation Assessment Detector (RAD) investigation. *Space Science Reviews*, *170*(1-4), 503–558. https://doi.org/10.1007/s11214-012-9913-1

Hassler, D. M., Zeitlin, C., Wimmer-Schweingruber, R. F., Ehresmann, B., Rafkin, S., Eigenbrode, J. L., et al. (2014). Mars's surface radiation environment measured with the Mars Science Laboratory's Curiosity rover. *Science*, *343*(6169), 1244797. https://doi.org/10.1126/science.1244797

ICRP (2010). Conversion coefficients for radiological protection quantities for external radiation exposures. ICRP publication 116. *Annals of the ICRP*, *40*(2-5), 1–257.

Le Deit, L., Mangold, N., Forni, O., Cousin, A., Lasue, J., Schröder, S., et al. (2016). The potassic sedimentary rocks in Gale crater, Mars, as seen by ChemCam on board Curiosity. *Journal of Geophysical Research: Planets*, *121*, 784–804. https://doi.org/10.1002/2015JE004987

Léveillé, R. J., & Datta, S. (2010). Lava tubes and basaltic caves as astrobiological targets on Earth and Mars: A review. *Planetary and Space Science*, *58*(4), 592–598. https://doi.org/10.1016/j.pss.2009.06.004

Lewis, S. R., Collins, M., Read, P. L., Forget, F., Hourdin, F., Fournier, R., et al. (1999). A climate database for Mars. *Journal of Geophysical Research: Planets*, *104*(E10), 24,177–24,194. https://doi.org/10.1029/1999JE001024

Manger, G. E. (1963). Porosity and bulk density of sedimentary rocks. Washington, D.C.

Matthiä, D., Ehresmann, B., Lohf, H., Köhler, J., Zeitlin, C., Appel, J., et al. (2016). The Martian surface radiation environment—A comparison of models and MSL/RAD measurements. *Journal of Space Weather and Space Climate*, *6*, A13. https://doi.org/10.1051/swsc/2016008

Mitrofanov, I. G., Litvak, M. L., Kozyrev, A. S., Sanin, A. B., Tret'yakov, V. I., Grin'kov, V. Yu., et al. (2004). Soil water content on Mars as estimated from neutron measurements by the HEND instrument onboard the 2001 Mars Odyssey spacecraft. *Solar System Research*, *38*(4), 253–257.

O'Neill, P. M. (2010). Badhwar–O'neill 2010 galactic cosmic ray flux model revised. *IEEE Transactions on Nuclear Science*, *6*(57), 3148–3153. https://doi.org/10.1109/TNS.2010.2083688

Orosei, R., Lauro, S. E., Pettinelli, E., Cicchetti, A., Coradini, M., Cosciotti, B., et al. (2018). Radar evidence of subglacial liquid water on Mars. *Science*, *361*(6401), 490–493. https://doi.org/10.1126/science.aar7268

Saganti, P. B., Cucinotta, F. A., Wilson, J. W., Simonsen, L. C., & Zeitlin, C. (2004). Radiation climate map for analyzing risks to astronauts on the Mars surface from galactic cosmic rays. *Space Science Reviews*, *110*(1), 143–156. https://doi.org/10.1023/B:SPAC.0000021010.20082.1a

Simpson, J. A. (1983). Elemental and isotopic composition of the galactic cosmic rays. *Annual Review of Nuclear and Particle Science*, *33*, 323–382. https://doi.org/10.1146/annurev.ns.33.120183.001543

Sullivan, J. D. (1971). Geometric factor and directional response of single and multi-element particle telescopes. *Nuclear Instruments and Methods*, *95*(1), 5–11. https://doi.org/10.1016/0029-554X(71)90033-4

Wan, L., Wendner, R., & Cusatis, G. (2016). A novel material for in situ construction on Mars: Experiments and numerical simulations. *Construction and Building Materials*, *120*, 222–231. https://doi.org/10.1016/j.conbuildmat.2016.05.046

Wänke, H., Brückner, J., Dreibus, G., Rieder, R., & Ryabchikov, I. (2001). Chemical Composition of Rocks and Soils at the Pathfinder Site. *Space Science Reviews*, *96*, 317–330. https://doi.org/10.1023/A:1011961725645